Electronic structure and scanning tunnelling microscope images of missing-atom defects on

MoS_2 and $MoTe_2$ surfaces

Electronic structure and scanning tunnelling microscope images of missing-atom defects on MoS$_2$ and MoTe$_2$ surfaces

J C Caulfield and A J Fisher

Department of Physics and Astronomy, University College London, Gower Street, London
WC1E 6BT, UK

Abstract.   Missing-atom defects on the transition metal dichalcogenides MoS$_2$ and MoTe$_2$ have been studied using the projector augmented-wave method, based on *ab initio* density functional theory. The presence of the vacancies results in localized electronic states in the surface band gap which can affect the STM image, and on the basis of our results we believe that the hole and trimer defects such as those observed by Fuchs *et al* could be explained by single-missing-chalcogen and single-missing-metal-atom defects respectively. It is found that the chalcogen vacancy systems behave in a similar way for both MoS$_2$ and MoTe$_2$; however, the system of MoTe$_2$ with a metal vacancy is discovered to be a Jahn–Teller system, while the equivalent MoS$_2$ system is not. The effects that this has on the atomic and electronic structure and the STM images are discussed.

1. Introduction

The continuing drive towards smaller electronic devices and nano-scale machinery has led to surface science becoming an ever-more-popular area of study, with particular attention being paid to nano-scale surface modification with scanning probe microscopes [7, 6, 19, 11]. The transition metal dichalcogenides (TX$_2$ where T represents the transition metal and X the chalcogen) are ideal materials for these kinds of study. The TX$_2$ family form in either a planar or a buckled, layered hexagonal structure with their conducting properties ranging from semiconducting (e.g. MoS$_2$, MoTe$_2$, WSe$_2$) to metallic (e.g. WTe$_2$). Both MoTe$_2$ and MoS$_2$ form in the planar hexagonal form shown in figure 1. Individual TX$_2$ layers are weakly Van der Waals bonded such that there is little resistance to layers sliding over each other, and atomically flat surfaces may be produced by cleaving. Consequently the TX$_2$ family make extremely good solid lubricants [5], and are ideal surfaces on which to carry out adsorption studies [10, 4]. In addition, the presence of the transition metal means that they can also act as catalysts. It is therefore important that we understand the behaviour of the surface, and it is to this end that many experimental and theoretical studies have been carried out. Another interesting feature restricted to metallic TX$_2$ is the existence of charge-density waves (long-wavelength correlations in electronic density); they are under study by several STM teams [9, 14].

The chemical, physical, and electronic properties (including the bulk and surface band structures) of these materials have been extensively studied [3, 13], and the members of the family share a number of common properties. There are also many groups using STMs
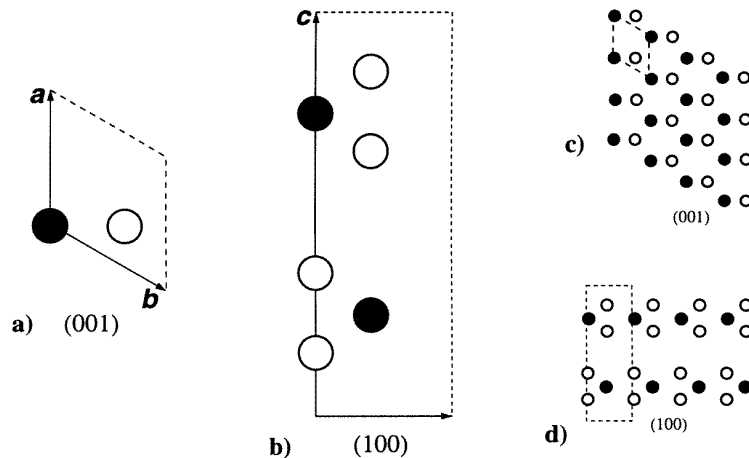
Figure 1. Schematic diagrams of the atomic structure of the planar transition metal dichalcogenides: (a) shows the unit cell in the (001) plane; (b) shows the unit cell in the (100) plane; and (c) and (d) show the tessellated structure in the same planes.

to examine the surfaces under various conditions; however, interpretation of STM images on any surface has always been problematic—and the transition metal dichalcogenides are no exception to this. There is an ongoing debate as to whether the peaks in the filled-state images of the TX_2 surfaces are due to the metal atoms, whose d levels provide most of the density of states at the top of the valence band, or the chalcogen atoms, which are physically closer to the tip. Simulation studies [13, 22, 18] are providing insight into the problem, and it is now agreed that under normal STM operating conditions it is probably the surface chalcogen atoms that are imaged. However, recent calculations on MoS_2, which included the tip explicitly [18], indicate that the image contrast will change if the tip–sample separation is small, such that it is neither the chalcogen nor the metal atoms being imaged. Experimental STM work such as that by Fuchs and Schimmel has been undertaken to study the effects of voltage pulsing on clean surfaces of WSe_2 [7, 6] and MoS_2 [8]. Fuchs and co-workers were able to create features on the surface ranging in size from ångströms (atom-sized holes and 'trimer' peaks) to several nanometres (blisters and rings). The underlying source of these structures and the mechanisms by which they are produced is open to debate, and provides an interesting problem for simulation. Whangbo *et al* [23] have carried out semi-empirical extended Hückel tight-binding calculations on the MoS_2 surface with point defects, and produced STM images which could explain the structures.

Here we report on *ab initio* electronic structure calculations of single-neutral-missing-atom defects on both MoS_2 and $MoTe_2$, expanding on the work of Whangbo *et al* [23] to include atomic relaxation and a better description of the wavefunctions. We use the results to address the problem of the origin of the point-like hole defects and the trimer-like peak defects, and find that they could be explained by single missing chalcogen and metal atoms respectively. We also find that $MoTe_2$ with a metal vacancy is a Jahn–Teller system, in contrast to the equivalent MoS_2 system. The methods used and the simulation details are described in section 2, and the results are presented in section 3 which is divided into four subsections, concerning: the bulk, the perfect surface, the missing-chalcogen-atom defects, and the two transition metal vacancy simulations. The conclusions that we have drawn from our study, and some recommendations for possible further work, can be found in section 4.

2. Methods

2.1. Electronic structure

In order to establish the ground-state electronic and ionic configuration, the projector augmented-wave (PAW) method developed by Blöchl [1] was used. The present implementation of the PAW method relies on density functional theory (DFT) within the local density approximation (LDA) [12], and utilizes the Perdew and Zunger [16] parametrization for the exchange–correlation term. In principle, DFT will produce the exact ground-state atomic positions and total charge density and should be able to cope with the Jahn–Teller effect in the correct manner; DFT and the LDA have been used by others to study Jahn–Teller systems with no unexpected problems [20]. What DFT does not strictly do is provide a method for calculating the STM images—that would require a knowledge of the electronic density of states as a function of energy. Here, we assume that the calculated Kohn–Sham eigenvalues and eigenstates determine the electron transport. The valence wavefunctions are expanded in plane waves, as in most conventional pseudopotential codes, with an additional atom-centred basis set making the PAW method an 'all-electron' (AE) method, i.e., the Kohn–Sham eigenfunctions are stored in their entirety, and the self-consistent potential is calculated from the full charge density. The core electrons are treated within the frozen-core approximation.

In the PAW representation, the AE wavefunctions $|\Psi\rangle$ are written as

$$|\Psi\rangle = |\tilde{\Psi}\rangle + \sum_i [|\phi_i\rangle - |\tilde{\phi}_i\rangle]\langle \tilde{p}_i|\tilde{\Psi}\rangle \tag{1}$$

where $|\tilde{\Psi}\rangle$ is the corresponding pseudowavefunction. The $|\tilde{p}_i\rangle$ are projector functions obeying $\langle \tilde{p}_i|\tilde{\phi}_j\rangle = \delta_{ij}$, and the $|\phi_i\rangle$ and $|\tilde{\phi}_i\rangle$ are atom-centred partial waves such that within some augmentation region Ω_R the AE wavefunction can be expanded as

$$|\Psi^{(1)}\rangle = \sum_i |\phi_i\rangle\langle \tilde{p}_i|\tilde{\Psi}\rangle \tag{2}$$

and the pseudowavefunction is expanded as

$$|\tilde{\Psi}^{(1)}\rangle = \sum_i |\tilde{\phi}_i\rangle\langle \tilde{p}_i|\tilde{\Psi}\rangle. \tag{3}$$

Outside the augmentation region, $|\tilde{\Psi}\rangle$ is equal to $|\tilde{\Psi}^{(1)}\rangle$.

There are a number of advantages associated with the PAW method: it is useful when simulating transition metals for which it is traditionally difficult to develop pseudopotentials owing to the rapidly varying valence wavefunctions near the atomic core; it is also useful for the study of hyperfine properties [17], where the electron spin density near the nucleus is important; finally, the atom-centred projector functions, which have the character of spherical harmonics, provide a convenient method for determining the orbital nature of the electrons associated with a particular atom. The Car–Parrinello (CP) algorithm [2] is used to relax the electronic and ionic degrees of freedom into their ground states simultaneously. The CP Lagrangian is set up in terms of the pseudowavefunctions, just as in the conventional CP method, with the parts of the calculation involving the pseudopotentials replaced by a series of transformations mapping the pseudowavefunctions to the AE wavefunctions [1]; the transformations are carried out on a radial grid about each atom. To improve the memory and CPU efficiency of the code, the implementation used here only allows the wavefunctions to be calculated at points in the reciprocal cell where the wavefunctions are purely real. The benefits of this are that larger systems may be studied, but the side-effect is that the full band structure cannot be obtained.
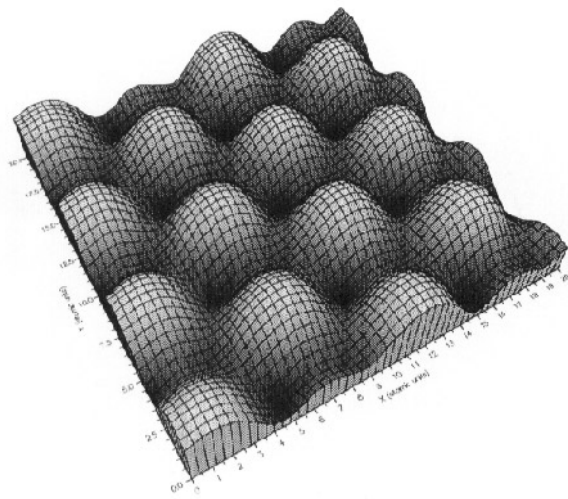
(a)
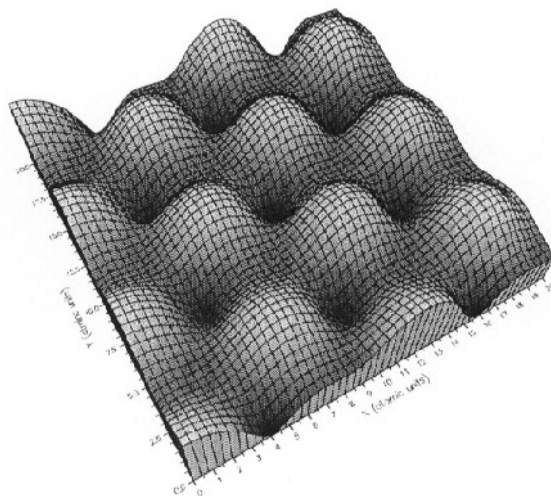
(b)

Figure 2. Perfect-surface STM images for (a) MoS_2 and (b) $MoTe_2$. The grey-scale represents a range of tip–surface separations between 0.91 and 2.04 Å for MoS_2 and 1.31 Å and 2.47 Å for $MoTe_2$. The peaks in the image occur above the chalcogen atoms as expected. See section 2.2 for details of the image calculations.

Since the PAW code uses plane waves to describe the wavefunctions, there is an inbuilt periodicity in all three basis vector directions for any system studied. This is ideal for simulating bulk properties, but means that surfaces must be approximated by slabs of finite thickness in a cell expanded in the direction perpendicular to the surface. The choice of slab thickness and cell height will vary depending on the system in question; the general rule is that the slab must be thick enough and the distance between slabs in adjacent cells

large enough that there are no interactions between the opposite surfaces.

Charge-density isosurfaces are used throughout this paper for visualizing the shape of the gap states (see section 3.3); for each set of diagrams associated with a single defect system, the isosurfaces are taken at the same charge per state, chosen arbitrarily to show the shape and localization.

2.2. STM images

The tunnelling current between the STM tip and the sample depends on many factors, such as the tip and sample geometries, their electronic structure, and the shape of the barrier between them. As a result of this it is difficult to predict exactly what the STM image should be for a given surface. All STM images presented here were obtained using the Tersoff–Hamann approximation [21]. In the Tersoff–Hamann approximations the surface is treated 'exactly' (i.e., within the LDA in the present calculation), the tip is assumed to be a spherical potential well where the s state provides the dominant contribution to the tunnelling, and perturbation theory is assumed valid. By expanding the surface wavefunctions as plane waves and the tip wavefunctions as spherical waves, we arrive at a tunnelling current of the form

$$ I \propto \int_{E_F - eV}^{E_F} dE \ \rho(r_0, E) \tag{4} $$

where r_0 is the position of the centre of the spherical well, V is the applied bias, and $\rho(r, E)$ is the density of surface states at position r and energy E.

There are several problems associated with this approximation: tip–sample interactions are completely ignored, and any localized gap states which may be present are assumed to contribute fully to the tunnelling current. Although tip–sample interactions are now considered to be important in many cases, this is probably not so under normal imaging conditions for the transition metal dichalcogenides where the surface is highly inert with no dangling bonds. The mechanism via which localized gap states/surface states contribute to the tunnelling current, if at all, is a topic of discussion [15], and whilst it is unlikely that the Tersoff–Hamann model treats these states correctly, it does produce useful first approximations to STM images which often bear close resemblance to experimental ones. One further approximation appears in our STM image calculations: the surface calculations presented here produce wavefunctions only at the Γ point of our supercell, and we therefore have no means by which to calculate the correct local density of states. The effects of dispersion are approximated by convolving the eigenvalues with a Lorentzian according to

$$ \rho(r, E) = \frac{1}{\pi} \lim_{\eta \to 0} \sum_n \frac{\eta}{(E - E_n)^2 + \eta^2} |\tilde{\Psi}_n\rangle\langle\tilde{\Psi}_n| \tag{5} $$

where the summation is over the eigenstates $|\tilde{\Psi}_n\rangle$, E_n are the eigenvalues of state n, and the parameter η determines the broadening of the states. Owing to its localization within Ω_R, the core charge does not contribute to the STM image under the Tersoff–Hamann approximation.

All images presented here are constant-current images for a simulated applied bias of 0.8 V (sample negative, i.e., tunnelling out of the sample surface) with a Lorentzian broadening (η) of 0.6 eV. The tip–sample separations referred to in the diagram captions are the distances between the centre of the STM 'tip' and the topmost chalcogen atoms of the surface. For the case of the vacancy defect STM images (and charge-density isosurfaces), the vacancy is always located at the centre of the image (box).
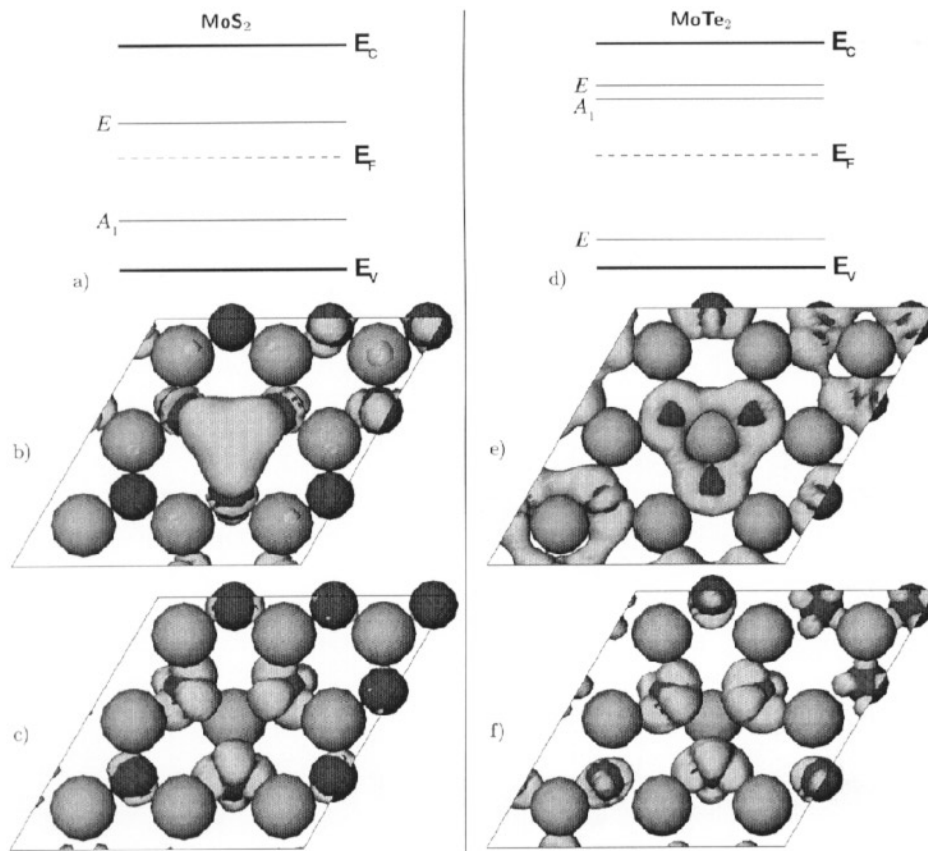
Figure 3. Eigenvalues and charge-density isosurfaces for the filled and empty gap states of MoS$_2$ and MoTe$_2$ with a chalcogen vacancy in the top chalcogen layer at the centre of the cell. (a) MoS$_2$ gap-state eigenvalues; (b) the MoS$_2$ filled-gap-state charge-density isosurface (0.003 au); (c) the MoS$_2$ empty-gap-state charge-density isosurface (0.006 au); (d) MoTe$_2$ gap-state eigenvalues; (e) the MoTe$_2$ filled-gap-state charge-density isosurface (0.003 au); and (f) the MoTe$_2$ empty-gap-state charge-density isosurface (0.006 au). The small dark and large lighter spheres represent the metal and chalcogen atoms respectively.

Table 1. Comparison of calculated and experimental bond lengths for bulk MoS$_2$ and MoTe$_2$.

Material	Bulk bond length (Å)	
	Calculated	Experiment
MoS$_2$	2.414	2.42
MoTe$_2$	2.721	2.71

3. Simulation results

3.1. Bulk

The projectors were tested in bulk MoS$_2$ and MoTe$_2$ simulations containing a single unit cell (6 atoms, 36 valence electrons) with the wavefunctions calculated at 8 k-points (Γ, M,

L and A where $e^{ik \cdot R}$, for all lattice vectors R, is real), and plane-wave cut-offs of 15 Ryd. Table 1 shows the optimized bond lengths, which are within 1% of the experimentally determined values; no attempt was made to optimize the cell parameters. There was good agreement between band structures from other similar calculations [13, 3] and the points available from these calculations.

3.2. Perfect surface

The surface simulations were based on a 3×3 $MoS_2/MoTe_2$ single-layer supercell (27 atoms, 162 valence electrons) with a *c*-dimension roughly equal to that of the bulk cell. Plane-wave cut-offs of 15 Ryd (tested for convergence to 25 Ryd) were used.

The single-slab approximation to a surface has been used by other groups [13], and is considered to be a reasonable one given that the interlayer interactions are small. The effective distance between adjacent surfaces (present because of the periodic boundary conditions) is large enough that there is no interaction between them.

Upon relaxation, the metal–chalcogen bond lengths (initially set to their bulk values) changed to 2.402 Å for MoS_2 and 2.715 Å for $MoTe_2$—a change of less than half a per cent of the calculated bulk values. This is further confirmation that, even in the bulk, the interaction between slabs is not large, and lends credibility to the single-slab surface approximation.

Figure 2 shows the calculated STM images for both MoS_2 and $MoTe_2$. Apart from the cell dimensions, the two are almost indistinguishable, with the peaks occurring above the surface chalcogen atoms as expected [13, 18]. It should be noted that recent calculations by Altibelli *et al* [18] on the MoS_2 surface which include the STM tip explicitly report that for tip–sample separations less than ~4.2 Å on MoS_2, the brightest point on the image does not occur at either the Mo or the S site. However, we do not have tips in any of our calculations, and we find that there is no significant separation dependence of the STM images within the range available to us—the images that we obtain are those predicted in [18] for larger (i.e., experimental) tip–sample separations.

3.3. Chalcogen vacancy

A chalcogen vacancy defect was simulated by removing a chalcogen atom along with its six valence electrons from the top layer (i.e. the side on which the STM images are taken) of the 3×3 surface supercell described in section 3.2. Plane waves up to a cut-off of 15 Ryd were used to describe the pseudowavefunctions.

Table 2. The magnitudes of the lattice distortions for the chalcogen vacancy systems for the nearest-neighbour Mo and chalcogen atoms. The distortions are almost entirely within the *ab*-plane.

Material	Nearest-neighbour metal-atom displacement (Å)	Nearest-neighbour chalcogen-atom displacement (Å)
MoS_2	0.003	0.003
$MoTe_2$	0.301	0.090

Table 2 shows the magnitude of the relaxations of the atoms nearest the defect for the Γ-point calculation. Starting from the relaxed atomic coordinates, the MoS_2 electronic

structure was recalculated with four k-points (Γ and M), and it was found that the forces in the Γ-point calculation were converged to within 0.008 au (0.4 eV Å^{-1}). The relaxation about the defect is much larger in $MoTe_2$ than in MoS_2 (which barely changes from the perfect structure), but in both cases the C_{3v} symmetry about the defect is maintained with the majority of the relaxation occurring in the *ab*-plane. Creation of the vacancy defect, and the associated removal of bonding electrons, causes localized electronic states to appear in the perfect-surface forbidden energy gap. Figure 3 shows the eigenvalues, degeneracies, and charge-density isosurfaces for the filled and empty gap states. The empty gap states are similar for MoS_2 and $MoTe_2$ (figures 3(c) and 3(f) respectively), being largely associated with the d orbitals of the metal atoms adjacent to the defect. The difference occurs in the filled gap states where for MoS_2 (figure 3(b)) the electrons are localized between the planes of the Mo and S atoms, directly below the vacancy. For $MoTe_2$ on the other hand, the charge is more diffuse, existing in the plane of the Mo atoms, concentrating in a ring encompassing the Mo atoms nearest the vacancy.

Figure 4 shows the calculated filled-state STM images and, although they are very similar (consisting unsurprisingly of peaks above the chalcogen atoms and a pit above the vacancy), it is possible to see a small bump in the central pit on the MoS_2 image which does not occur for $MoTe_2$; this difference can be attributed to the difference in the filled gap states. These images are similar to those obtained by Whangbo *et al* for MoS_2 with a sulphur vacancy. Furthermore, in STM experiments carried out by Fuchs *et al* [7], defects have been observed on WSe_2, and more recently on MoS_2 [8], which also look similar to those in figure 4—it seems likely that these defects are due to missing surface Se/S atoms.

3.4. Metal vacancy

The similarity of the results for the chalcogen vacancy for MoS_2 and $MoTe_2$ is not surprising, since all isostructural transition metal dichalcogenides have similar physical and chemical properties. However, our simulations on metal vacancies in MoS_2 and $MoTe_2$ indicate that these systems behave quite differently, and because of this they are discussed separately below.

3.4.1. MoS_2 with Mo vacancies.   As for the chalcogen defect systems, a 3×3 surface supercell was used with a plane-wave cut-off of 15 Ryd, and a single Mo atom, including its valence electrons, removed from the supercell. The relaxation of the lattice around the defect was minimal, with the nearest-neighbour S atoms moving away from the vacancy by 0.014 Å in the *ab*-plane, with a slight inwards relaxation in the *c*-direction. The D_{3h} symmetry about the defect was unchanged on relaxation.

Five gap states are apparent in this case: a doubly degenerate state below the Fermi level, and a singly and a doubly degenerate state above the Fermi level. Figure 5 shows the eigenvalues, degeneracies, and filled- and empty-gap-state charge-density isosurfaces. The filled-gap-state charge (figure 5(b)) is mostly associated with the dangling p orbitals on the S atoms adjacent to the vacancy. The empty-gap-state charge (figure 5(c)) is concentrated on the metal atoms adjacent to the vacancy.

3.4.2. $MoTe_2$ with Mo vacancies.   For the $MoTe_2$ system with a Mo vacancy, a 4×4 single-slab supercell was used with a plane-wave cut-off of 15 Ryd for the valence pseudowavefunctions. Initially, a 3×3 cell was used as for the other calculations, but it was found that $MoTe_2$ with a Mo vacancy was a Jahn–Teller system, and, because of this, the lattice relaxation was larger and of longer range than expected. The cell size was
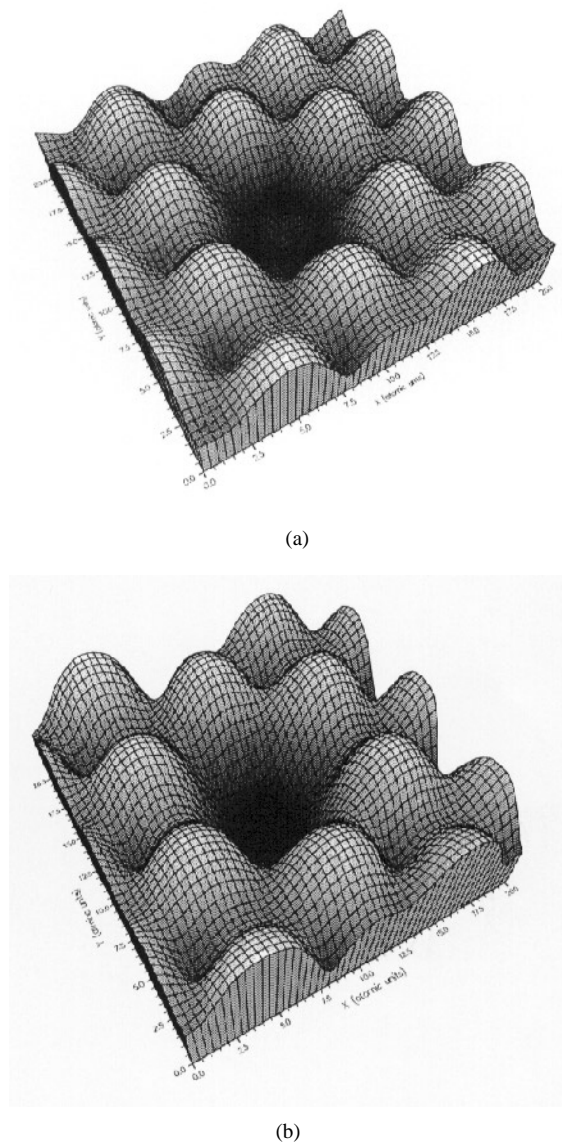
(a)

(b)

Figure 4. Calculated STM images for (a) MoS_2 and (b) $MoTe_2$ with a chalcogen vacancy located at the centre of the image. There is a slight bump in the central pit of the MoS_2 image which does not appear in the $MoTe_2$ image, due to the structure of the filled-gap-state charge density (figure 3(b), 3(e)) which is physically closer to the tip in MoS_2. The grey-scale represents a range of tip–surface distances between 1.1 and 3.4 Å for MoS_2, and 1.1 and 4.3 Å and $MoTe_2$.

increased to 4×4 to accommodate the relaxation and check that the Jahn–Teller effect was not due to the finite size of the cell.

Figure 6 shows the relaxed atomic structure overlaid on a shadow of the undistorted cell (i.e., before the atoms were allowed to move); the D_{3h} symmetry of the non-relaxed structure is reduced to C_2 upon relaxation. The largest displacements from the perfect-surface positions occur for the atoms nearest the vacancy: the nearest-neighbour Mo atoms
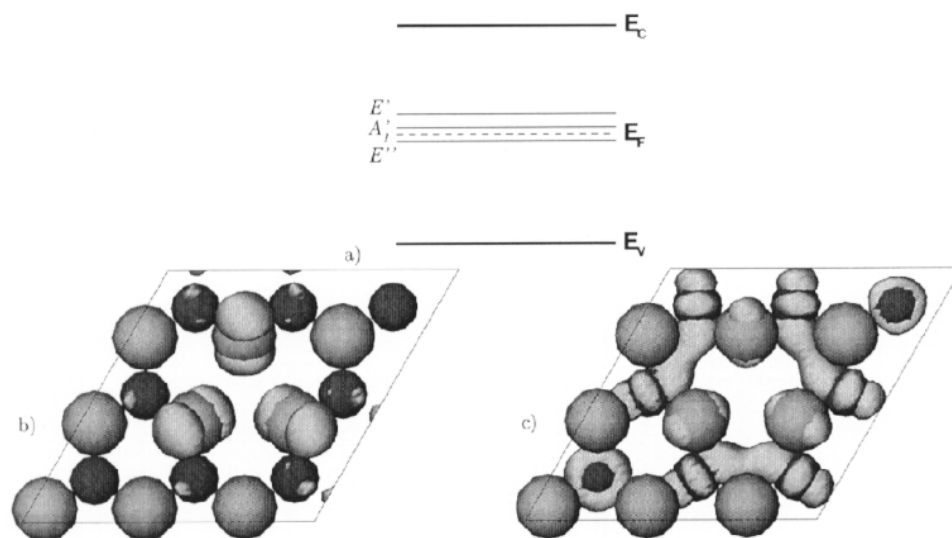
Figure 5. (a) Gap-state eigenvalues and degeneracies, (b) the filled-gap-state charge-density isosurface (0.0036 au), and (c) the empty-gap-state charge-density isosurface (0.0054 au) for MoS_2 with a Mo vacancy located at the the centre of the cell. The small dark and large lighter spheres represent the Mo and S atoms respectively.
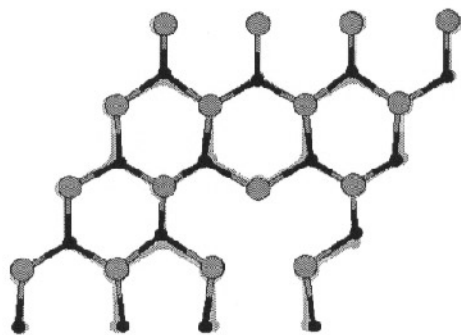

Figure 6. $MoTe_2$ atomic structure before and after atomic relaxation. The foreground (bold) image shows the relaxed, distorted structure, and is overlaid on a 'shadow' of the undistorted (i.e. perfect-surface) structure. The D_{3h} symmetry of the undistorted system is reduced to C_2 upon relaxation.

are displaced by 0.31 Å, and the nearest-neighbour Te atoms move 0.22 to 0.25 Å depending on their position relative to the C_2 axis. However, unlike in the other simulations described in this paper, the relaxation extends beyond the vacancy's nearest neighbours, with the second-nearest-neighbour Mo and Te atoms moving by 0.20 Å and 0.18 Å respectively.

The reason for this symmetry-breaking distortion becomes apparent upon examination of the electronic structure of the non-relaxed system. It is found that the lowest-energy electronic configuration in the case where the ions are fixed in their perfect-surface positions is one in which the two highest occupied eigenstates are equally (i.e., singly) occupied.
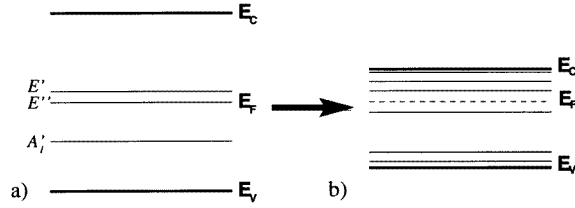
Figure 7. Ground-state eigenvalues for MoTe$_2$ with Mo vacancies: (a) with atoms in their perfect-surface positions, and (b) after atomic relaxation. There is an orbital degeneracy at the Fermi level in the non-relaxed system which leads to a Jahn–Teller distortion upon relaxation. The reduction of the band gap on relaxation is attributed to finite-size effects.

Figure 7(a) shows a schematic diagram (to scale) of the eigenvalues and degeneracies before and after atomic relaxation; before relaxation the A$'_1$ state is below the E$''$ state (cf. figure 5(a), where this situation is reversed) leaving a pair of singly occupied degenerate states at the Fermi level, making this a Jahn–Teller system.

Table 3. The average magnitude per atomic site of the projected distortions (equation (7)) in ångströms for each of the D$_{3h}$ representations. The A$'_1$ and E$'$ representations account for most of the total lattice relaxation (see also figure 8).

Atoms	A$'_1$	A$'_2$	E$'$	A$''_1$	A$''_2$	E$''$
Nearest-neighbour Mo	0.184	0.001	0.195	0.002	0.000	0.010
Nearest-neighbour Te	0.231	0.000	0.049	0.000	0.000	0.009
Second-nearest-neighbour Te	0.108	0.000	0.114	0.002	0.000	0.010

Examination of a table showing how the irreducible representations of the D$_{3h}$ group behave on reduction of the symmetry shows that the E$''$ state remains doubly degenerate until the symmetry is reduced to at least C$_{2v}$. Table 3 shows the magnitudes per atomic site of the symmetry-projected distortions for each of the six irreducible representations ν of the group D$_{3h}$. These are defined by

$$d^{(\nu)} = \frac{1}{n_a} \sum_i^{n_a} |R_i^{(\nu)}|^2 \tag{6}$$

where n_a is the number of sites in the shell under study (nearest neighbour, etc), and $R_i^{(\nu)}$ is the symmetry-projected distortion for representation ν at site i:

$$R_i^{(\nu)} = P^{(\nu)} R_i = \left[\frac{n_\nu}{g} \sum_{A \text{ in } \mathcal{G}} \chi^{(\nu)}(A) A \right] R_i \tag{7}$$

where n_ν is the dimension of representation ν in group $\mathcal{G}$, g is the order of $\mathcal{G}$, $\chi^{(\nu)}(A)$ is the character of A, and R_i is a column vector of all of the displacements of the atoms in the shell in question.

This shows that the distortion of the lattice is largely due to two modes: one which transforms like the identity representation A$'_1$ (figure 8(a)) and one which transforms according to the E$'$ representation (figure 8(b)). There is also a small contribution from the E$''$ representation, without which the symmetry would have been C$_{2v}$ as opposed to C$_2$, but this is more than an order of magnitude smaller than the A$'_1$ and E$'$ contributions and is invisible on the scale of figure 8.
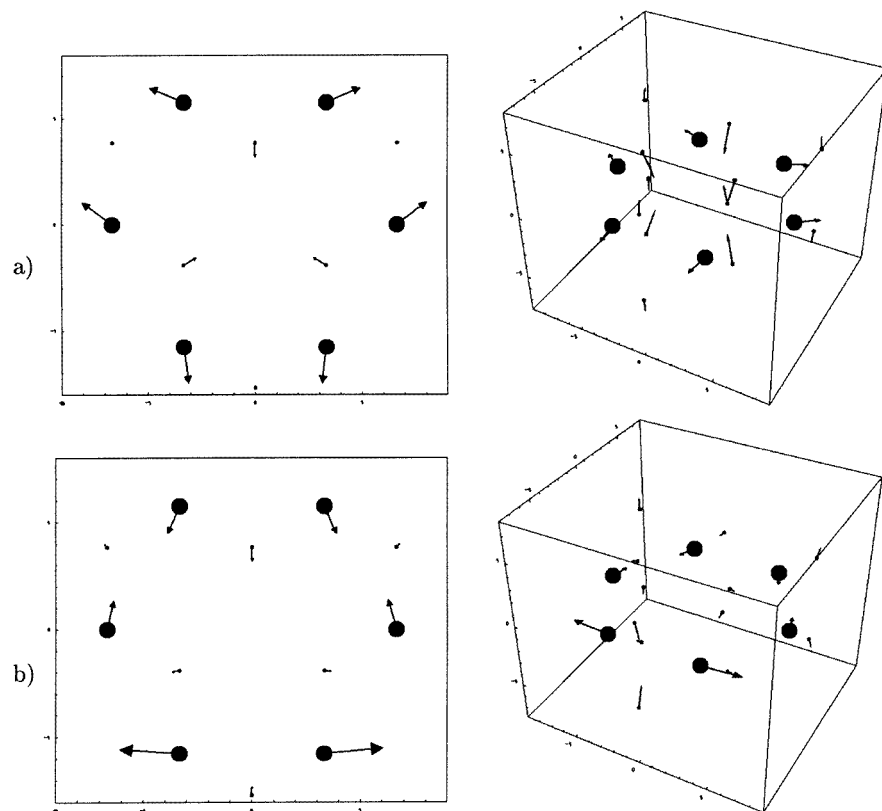
Figure 8. A vector diagram of the symmetry-projected distortions (equation (7)) for MoTe$_2$ with a Mo vacancy (centre of the box). Shown are (a) the A$_1'$ and (b) the E$'$ components (scaled ×5) for the nearest-neighbour Mo (large circles) and the first- and second-nearest-neighbour Te atoms (small circles). No other components show up on this scale (see table 3). The 2D images are viewed from above the *ab*-plane; the 3D versions are present to show the vertical component of the Te distortions.

Figure 9 shows the filled- and empty-gap-state charge densities for the system before and after atomic relaxation (the labelling of states as 'gap states' here is not precise, owing to the small separation between the band-edge and the gap states, and is based purely on their physical localization). Comparing the gap states of MoTe$_2$ (figure 9) with those of MoS$_2$ (figures 5(b), 5(c)) we see that they have a similar make-up in terms of atomic orbitals, but that the Jahn–Teller distortion of the MoTe$_2$ system results in a lowering of the electronic symmetry to C$_2$ and an exchange of the filled and empty gap states, i.e., the p states associated with the chalcogens are now above the Fermi level, whereas the states localized around the metal are below E_F.

3.4.3. STM images. Figure 10 shows the calculated filled-state STM images for both MoS$_2$ and MoTe$_2$ with a metal vacancy (at the centre of the image). The inversion of the filled and empty gap states between the two systems results in them having different Tersoff–Hamann STM images. The MoS$_2$ image has a trimer of brighter peaks associated with the S atoms adjacent to the vacancy in agreement with [23], whereas the nearest-neighbour Te atoms in
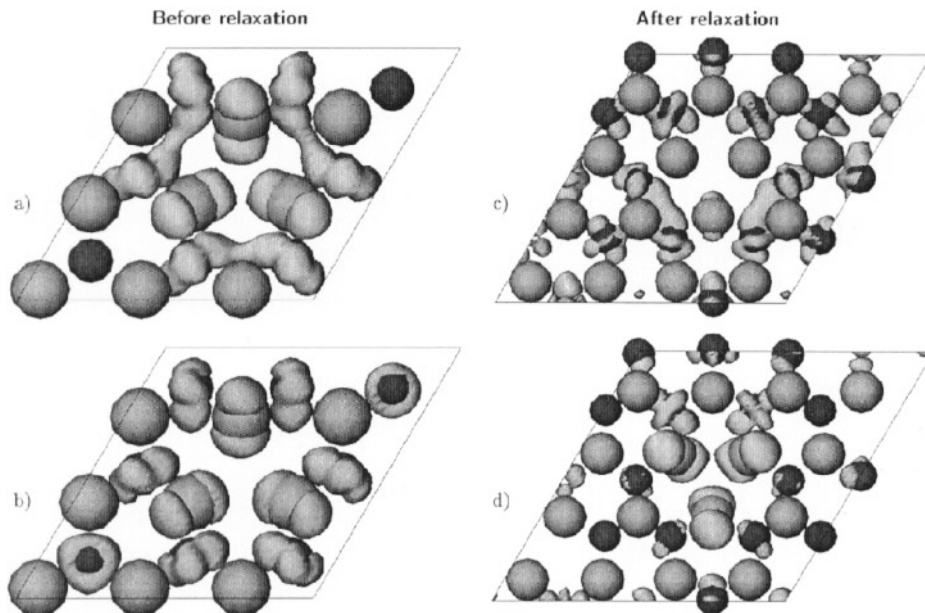
Before relaxation   After relaxation

Figure 9. The filled (top) and empty (bottom) gap states for MoTe$_2$ with a Mo defect located at the centre of the cell; (a) and (b) are for the undistorted geometry; (c) and (d) are for the relaxed geometry where there is an apparent reversal of states with respect to the equivalent MoS$_2$ system (figure 5). The isosurfaces were taken at 0.001 au/state. The small dark and large lighter spheres represent the Mo and Te atoms respectively.

the MoTe$_2$ image appear darker than the rest.

The previously mentioned STM experiments performed by Fuchs *et al* [7, 8] also show trimer-like defects similar to those seen here for MoS$_2$ with a metal vacancy (figure 10(a)) which, on the basis of this work, we believe may also be due to sub-surface metal vacancies.

4. Discussion and conclusions

We have used DFT within the LDA to study the electronic structure and STM images of MoS$_2$ and MoTe$_2$ surfaces, and have examined the effects of introducing both metal and chalcogen vacancy defects into the system. All of the simulations presented here were carried out on a 3×3 (4×4 for MoTe$_2$ with a Mo vacancy) single-slab supercell—taking into account the periodic boundary conditions, this implies a very high surface defect density for the vacancy calculations. However, we have shown that the atomic relaxation about the vacancies is small, and that the gap-state charge density is largely localized around the vacancy centre or immediately adjacent atoms, implying that the interaction between the defects is small, and lending credibility to the supercells used.

Fuchs *et al* have studied the effects of voltage pulsing with the STM tip on the surfaces of WSe$_2$ and MoS$_2$, and they have been able to produce many interesting features ranging in size from single-atom holes and trimer-atom peaks to rings several nanometres across. On the basis of the results of our defect calculations on MoS$_2$ (figures 4(a), and 10(a)) we believe that the observed single-atom holes and the trimer peaks are probably caused by surface chalcogen and sub-surface metal vacancies respectively. However, we find that
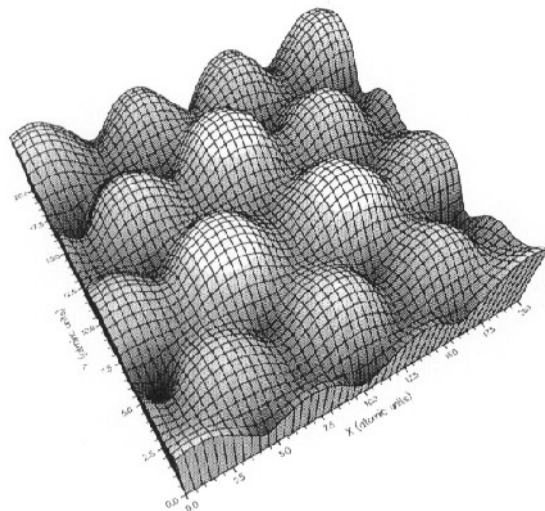
(a)
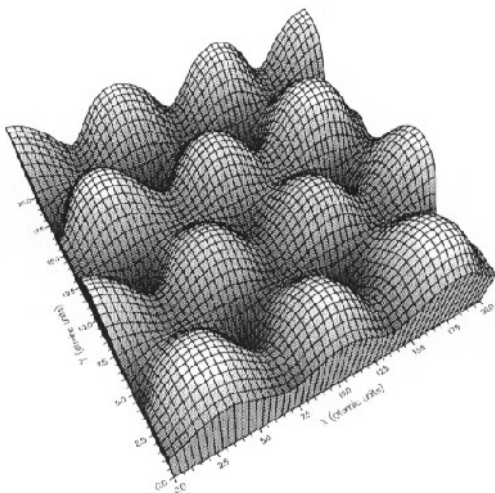
(b)

Figure 10. Calculated filled-state STM images for (a) MoS_2 and (b) $MoTe_2$ with a metal vacancy located below the surface at the centre of the image (see section 2.2 for details of the image calculation). The differences between the images can be attributed to the ordering and localization of the filled gap states: for MoS_2 these states are localized around the chalcogen atoms, whereas for $MoTe_2$ the filled states are localized around the metal atoms, which are physically further from the tip, and therefore do not contribute so strongly to the image within the Tersoff–Hamann approximation.

although the chalcogen defect systems behaved in qualitatively similar ways for MoS_2 and $MoTe_2$ (section 3.3), the different orderings of the gap states in the two metal defect systems causes a significant difference between their behaviours. In MoS_2 with a metal vacancy, the gap states below E_F are mainly associated with the p orbitals of the chalcogen atoms

adjacent to the vacancy, whereas those above E_F are largely metal d states. For MoTe$_2$ with a metal vacancy, on the other hand, we find that in the non-relaxed geometry the total gap-state charge density is similar to that of MoS$_2$, but the eigenstates are ordered differently, with a mixing of the filled and empty gap states; furthermore, there is an orbital degeneracy at the Fermi level, making MoTe$_2$ with a metal vacancy a Jahn–Teller system. Upon relaxation, the Jahn–Teller distortion of the MoTe$_2$ metal vacancy system reduces the symmetry about the defect from D$_{3h}$ to C$_2$, and this results in the inversion of the filled and empty gap states, with a slight mixing, compared to those of MoS$_2$. We have found no trace of any significant difference in the electronic structure (for example in the projected density of states) of the two perfect surfaces that might suggest why MoTe$_2$ with a metal vacancy is a Jahn–Teller system where the equivalent MoS$_2$ system is not. It would be interesting to see if the decomposition of the electronic states into atomic orbitals in a tight-binding calculation could help to give a qualitative picture of the phenomenon.

It would also be interesting to see whether the trimer-like defects experimentally observed on WSe$_2$ and MoS$_2$ can be created on MoTe$_2$ and imaged with the STM. In addition, it might be worth examining the effect of reversing the tip–sample bias on the STM images—this could be done by extending the current calculation to include more empty states. It seems reasonable to predict, on the basis of the fact that the perfect-surface images are similar for positive and negative bias [13], that the chalcogen vacancy images will not change much, and that a trimer peak will be seen in the surface-positive (empty-state) image for MoTe$_2$ with a Mo vacancy. The exact location of the trimer-producing gap states in energy appears to depend on the TX$_2$ system under consideration. The circumstances under which the defect becomes charged could also be important, especially for the Mo vacancy in MoTe$_2$, where the Te-related dangling-bond states are just above the Fermi level. In this case, a slight rise in the Fermi level at the surface (e.g. due to the presence of the tip) could change the charge state of the defect and hence the STM image.

Acknowledgments

References

[1] Blöchl P E 1994 *Phys. Rev.* B **50** 17 953
[2] Car R and Parrinello M 1989 *Simple Molecular Systems at Very High Densities* ed A Polian, P Loubeyre and N Boccara (Oxford: Plenum) pp 455–76
[3] Dawson W G and Bullet D W 1987 *J. Phys. C: Solid State Phys.* **20** 6159–74
[4] Fisher A J and Blöchl P E 1993 *Phys. Rev. Lett.* **70** 3263–6
[5] Fleischauer P 1987 *Thin Solid Films* **154** 309–22
[6] Fuchs H, Schimmel T, Akari S, Eng L M, Anders M, Lux-Steiner M and Dransfield K 1993 *Nanosources and Manipulation of Atoms Under High Fields and Temperatures: Applications* (Dordrecht: Kluwer Academic) pp 293–309
[7] Fuchs H, Schimmel T, Lux-Steiner M and Bucher E 1992 *Ultramicroscopy* **42–44** 1295–302
[8] Fuchs H 1996 private communication
[9] Garnaes J, Gould S A C, Hansma P K and Coleman R V 1991 *J. Vac. Sci. Technol.* B **9** 1032–5
[10] Hara M, Iwakabe Y, Tochigi K, Sasabe H, Garito A F and Yamada A 1990 *Nature* **344** 228–30
[11] Huang J, Sung Y and Lieber C M 1992 *Appl. Phys. Lett.* **61** 1528–30
[12] Jones R O and Gunnarsson O 1989 *Rev. Mod. Phys.* **61** 689–746
[13] Kobayashi K and Yamauchi J 1995 *Phys. Rev.* B **51** 17 085–95

[14] Liang X and Lieber C M 1991 *J. Vac. Sci. Technol.* B **9** 1044–7
[15] Lawunmi D and Payne M C 1995 *J. Phys.: Condens. Matter* **7** 5155–62
[16] Perdew J P and Zunger A 1981 *Phys. Rev.* B **23** 5048–79
[17] Probert M I J and Fisher A J 1996 *Chem. Phys. Lett.* **259** 271–5
[18] Altibelli A, Joachim C and Sautet P 1996 *Surf. Sci.* **367** 209–20
[19] Schimmel T, Kemnitzer R, Küppers J, Fuchs H and Lux-Steiner M 1995 *Thin Solid Films* **254** 147–52
[20] Tarnow E 1993 *J. Phys.: Condens. Matter* **5** 1863–976
[21] Tersoff J and Hamann D R 1985 *Phys. Rev.* B **31** 805–13
[22] Magonov S N and Whangbo M 1994 *Adv. Mater.* **5** 355–71
[23] Whangbo M H, Ren J, Magonov S N, Bengel H, Parkinson B A and Suna A 1995 *Surf. Sci.* **326** 311–26